Sensitivity of Climate Analogues to Problem-Specific Adjustments: A Case Study
Supplementary Material

Héloïse Allaman [a,*] , **Stéphane Goyette** [a] , **Pierre-Henri Dubuis** [b] , **Jérôme Kasparian** [a]

[a] *Group of Applied Physics and Institute for Environmental Sciences, University of Geneva, Bd. Carl-Vogt 66, 1205 Geneva, Switzerland*

[b] *Agroscope Changins, Rte de Duillier 60, 1260 Nyon, Switzerland*

[*] *Corresponding author*

E-mail: heloise.allaman@unige.ch, stephane.goyette@unige.ch, pierre-henri.dubuis@agroscope.admin.ch, jerome.kasparian@unige.ch

S1 Local temperature correction for sub-grid topography

To better represent vineyard-level climate conditions, we apply a temperature correction that accounts for sub-grid topographic features—namely, elevation, slope, and aspect—unresolved by the RCM.

The temperature correction due to elevation is the following:

$$T_{\text{vine}} = T_0 + \Gamma_e(z - z_0), \tag{S1.1}$$

with $\Gamma_e = -0.0065°\text{C/m}$ the environmental lapse rate (Peixoto and Oort, 1992), z the elevation of the vineyard, and T_0 and z_0 the interpolated values interpolated bilinearly from the four nearest grid points of a vineyard's location.

The correction due to the slope and aspect of the terrain is given by (Bennie et al., 2008):

$$T_{\text{slope}} = T_{\text{flat}} + a(1-\alpha)(R_{\text{sw}}^{\text{slope}} - R_{\text{sw}}^{\text{flat}}), \tag{S1.2}$$

with $a = 0.013$ a dimensionless coefficient considering a typical windspeed $u \geq 1$ m/s, $\alpha = 0.2$ the surface albedo of vineyards (Pieri and Gaudillère, 2015), T_{flat} the temperature on a flat surface receiving a net shortwave radiation flux $R_{\text{sw}}^{\text{flat}}$, and T_{slope} the temperature on a slope at the same location receiving a radiation flux $R_{\text{sw}}^{\text{slope}}$.

The total shortwave radiation provided by the climate model consists of both direct and diffuse components. Only the direct component is affected by terrain slope or the angle of incoming solar radiation, but is not provided by the climate model. To address this, we approximate the proportion of direct, Rayleigh, and Mie contributions.

Although Rayleigh scattering theoretically produces diffuse radiation, we make the simplifying assumption that the Rayleigh component behaves as direct radiation, thus contributes to the overall temperature corrections (Duffie and Beckman, 2013). We approximate the Mie scattering by assuming that the cloud cover is constant throughout the day. The direct incoming solar radiation at a given time t is given by $R_{\text{dir}}(t) = (1-c)\cdot R_{\text{cs}}(t)$, with c in [0 – 1] the cloud cover, and $R_{\text{cs}}(t)$ the clear sky solar radiation. It is given by geometry:

$$R_{\text{cs}}^{\text{flat}}(t) = F_s \cdot r^{*2} \cdot \psi^{\sec Z(t)} \cdot \cos Z(t), \tag{S1.3}$$

with $F_s = 1370$ Wm^{-2} the solar constant, r^* the relative deviation from the Earth-Sun distance with regard to its average value, $\psi = 0.75$ the atmosphere transmitivity at mid-latitudes and $Z(t)$ the solar zenith angle. The direct solar radiation on a flat surface is then estimated using:

$$R_{\text{dir}}^{\text{flat}}(t) = \frac{\bar{R}}{\bar{R}_{\text{cs}}} R_{\text{cs}}^{\text{flat}}(t), \tag{S1.4}$$

with $\bar{R}$ the daily average solar radiation obtained from the RCM given the cloud cover and $\bar{R}_{\text{cs}}$ the clear sky solar radiation on a flat surface averaged over 24 hours.

The solar radiation $R_{\text{sw}}^{\text{slope}}$ received on a slope S with aspect Ω depends on the position of the sun relative to the terrain Oke (1987). It varies with the time t of the day:

$$R^{\text{slope}}_{\text{dir,cs}}(t) = \frac{R^{\text{flat}}_{\text{dir,cs}}(t)}{\cos Z(t)} \big(\cos Z(t) \cos S + \sin Z(t) \sin S \cos \left(\Omega_S(t) - \Omega\right) \big), \tag{S1.5}$$

with $\Omega_S(t)$ the solar azimuth and $R^{\text{flat}}_{\text{dir,cs}}$ the direct component of the solar clear sky incoming radiation on a flat surface, given by Eq. S1.3.

The solar azimuth and zenith angles are calculated using spherical geometry (Oke, 1987), and depend on the latitude, date, and time of day. The daily minimum temperature, typically occurring around sunrise, is largely unaffected by slope, whereas the daily maximum temperature correction is greatest, as it coincides with peak solar radiation near solar noon. To estimate this correction, we use the maximum solar radiation, when the zenith angle is at its minimum. The correction for the daily mean temperature is then obtained by computing hourly corrections using Eq. S1.5 and averaging over 24-hour.

To match the projected climate of vineyards with present-day computational grid points, we apply topographic corrections to the grid point temperatures. Each RCM cell covers approximately 140 km^2 and includes sub-grid-scale topographic features. We aim to identify climate analogues at the most likely location for vineyards, i.e., on south-facing slopes. Therefore, within each grid cell, we select the location that yields the maximum correction to the daily maximum temperature. Note however that this method may also highlight locations that could become excessively hot for viable viticulture, potentially limiting suitable analogue matches.

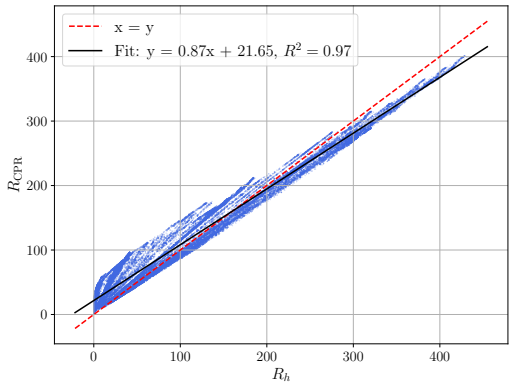

Fig. S1.1 Scatter plot of the hourly mean estimate $R_h(t)$ of a sample of vineyards computed using the CPR model compared to Eq. S1.4

Figure S1.1 compares the outputs of Eqs. S1.4 and S1.5 with those of the Collares-Pereira and Rabl (CPR) model for the year 2006 across the vineyards. The two models show a strong correlation ($R^2 = 0.97$). The linear relationship between them, $R_{\text{CPR}} = 0.87 \cdot R_h + 21.65$, is consistent with the average fit obtained between the CPR model and on-site measurements over Europe ($R_{\text{CPR}} = 0.89 \cdot R_{\text{observed}} + 27.66$; Kambezidis, 2025). As sub-grid observations are unavailable to directly evaluate our model, we assess its performance

indirectly by combining these two relationships, yielding $R_{\mathrm{h}} = 1.02 \cdot R_{\mathrm{observed}} + 6.91$. The slope close to unity indicates that the model defined by Eqs. S1.4 and S1.5 slightly outperforms the CPR model over vineyard areas.

S2 Bioclimatic indices

This section provides the expressions of the six bioclimatic indices used in this work. Several of them are computed starting from bud break day (BB), estimated using growing degree-days, starting from January 1st (Garcia de Cortazar-Atauri et al., 2009):

$$\sum_{01\ \mathrm{Jan.}}^{BB} \max\left(T_{\mathrm{d}} - 5°\mathrm{C},\ 0°\mathrm{C}\right) \geq 275°\mathrm{C}, \tag{S2.1}$$

with T_{d} the daily mean temperature. The Huglin index is computed from bud break day to harvest (end of September) (Huglin, 2003; Hall and Jones, 2010):

$$I_{\mathrm{HI}} = \sum_{BB}^{30\ \mathrm{Sep.}} \max\left[\left(\frac{T_{\mathrm{d}} + T_{\mathrm{max,d}}}{2} - 10°\mathrm{C}\right), 0\right] \cdot \left(2.55 \cdot 10^{-4} \cdot L_s + 0.278\right), \tag{S2.2}$$

with $T_{\mathrm{max,d}}$ the maximum daily temperature and L_s the total season day-length, i.e. the sum of daily daylight hours from bud break day to the end of September. The two other indices related to vine growth are the number of frost and of extreme heat days respectively, given by:

$$I_{\mathrm{frost}} = \sum_{BB}^{31\ \mathrm{May}} \chi(T_{\mathrm{min,d}} < -2°\mathrm{C}), \tag{S2.3}$$

$$I_{\mathrm{heat}} = \sum_{BB}^{30\ \mathrm{Sep.}} \chi(T_{\mathrm{max,d}} > 35°\mathrm{C}), \tag{S2.4}$$

with $T_{\mathrm{min,d}}$ the daily minimum temperature and χ the indicator function, being 1 the condition in parenthesis is fulfilled and 0 otherwise. The flavescence dorée index is given by (Sneiders et al., 2019):

$$I_{\mathrm{FD}} = \sum_{year} \max\left[\left(\frac{T_{\mathrm{d}} + T_{\mathrm{max,d}}}{2} - 8.7°\mathrm{C}\right), 0\right]. \tag{S2.5}$$

The downy mildew index depend on the hourly leaves wetness, which is not provided as a climate model output. We therefore estimate a leaf wetness function on the basis of the hourly temperature (Wann et al., 1985):

$$T(t) = \begin{cases} T_{\mathrm{min,d}} + (T_{\mathrm{max,d}} - T_{\mathrm{min,d}}) \sin\left[\frac{\pi(t-t_{\mathrm{r}})}{l+2\alpha}\right] & t_{\mathrm{r}} + \leqslant t \leqslant t_{\mathrm{s}}, \\ \\ T'_{\mathrm{min,d}} + [T(t_{\mathrm{s}}) - T'_{\mathrm{min,d}}] \exp\left[-\frac{\gamma(t-t_{\mathrm{s}})}{24-l}\right] & t_{\mathrm{s}} \leqslant t < t'_{\mathrm{r}}, \end{cases} \tag{S2.6}$$

with t_r and t_s the sunrise and sunset times, $\alpha = 1.2$ h the time lag between time where maximum temperature is reached and midday (Holmes et al., 2013), l the day length, and $\gamma = 2.2$ the decay parameter, determining the rate of temperature change between sunset and sunrise. The minimum temperature is assumed to occur at $t = t_\mathrm{r}$, i.e. at sunrise. Prime indices indicate data from the following day. One can then obtain the time-dependant relative humidity RH(t) using the saturated water vapour pressure at the dew point and that of the air (Zito et al., 2020). The downy mildew index corresponds to the number of risk days throughout the growing season, beginning from BBCH13 (i.e., the three-leaf stage, which is estimated to occur five days after BB (Garcia de Cortazar-Atauri et al., 2009)):

$$I_\mathrm{DM} = \sum_{\mathrm{BBCH13}}^{\text{30 Sep.}} \mathrm{R}_d, \tag{S2.7}$$

with the daily risk of infection R_d depending on the daily precipitation pr and on the dew point temperature T_dew:

$$\mathrm{R}_d = \begin{cases} 0 & T_\mathrm{d} < 12°\mathrm{C}, \\ 1 & T_\mathrm{d} \geq 12°\mathrm{C} \text{ and } pr \geq 1 \text{ mm/d}, \\ \frac{1}{24}\sum_h \chi(T(h) - T_\mathrm{dew}(h) \leq 5°\mathrm{C}) & \text{otherwise.} \end{cases} \tag{S2.8}$$

The powdery mildew index, which indicates the number of days during the growing season that are favourable for a powdery mildew infection, is given by (Walter Kast, 2009):

$$I_{PM} = \sum_{\mathrm{BBCH13}}^{\text{30 Sep.}} (f_\mathrm{temp} \cdot f_\mathrm{hum} - f_\mathrm{wet}) \cdot f_\mathrm{on}, \tag{S2.9}$$

with all functions normalised to 1. f_temp and f_hum are functions describing the optimal temperature and humidity conditions required for the disease to develop (Carroll and Wilcox, 2003; Walter Kast, 2009):

$$f_\mathrm{temp} = 1.63 \cdot (0.11\ T_\mathrm{d} - 0.0025\ T_\mathrm{d}^2 - 0.6), \tag{S2.10}$$

$$f_\mathrm{hum} = \min\left(\frac{\mathrm{RH_d}}{85}, 1\right), \tag{S2.11}$$

with $\mathrm{RH_d}$ the daily mean relativity humidity. f_on describes the ontogenetic resistance of grapes (Walter Kast, 2009):

$$f_\mathrm{on} = \min\left(\frac{1}{100}\left(0.0002D^3 + 176.6\sqrt{D} - 114.9\ln D - 14D - 66\right), 0.2\right), \tag{S2.12}$$

with D the number of days past BBCH13. The function f_wet describes leaves wetness, and is given by (Walter Kast, 2009):

$$f_\mathrm{wet} = \frac{3}{1 + e^{-0.5(\mathrm{pr}-6.25)}} \cdot \frac{1}{24}\sum_h \chi(T(h) - T_\mathrm{dew}(h) \leq 5°\mathrm{C}). \tag{S2.13}$$

Temperature corrections are applied before computing the bioclimatic indices, and therefore, they are included in the hourly relative humidity. However, these corrections are not considered in the daily relative humidity used in Eq. S2.11.

S3 Principal Component Analysis and Similarity Index

Bioclimatic indices with temperature correction						
Variable	**PC1**	**PC2**	**PC3**	**PC4**	**PC5**	**PC6**
Huglin index	0.54	0.19	0.06	0.08	0.17	-0.79
Flavescence dorée	0.49	0.40	0.11	-0.07	0.54	0.55
Extreme heat days	0.50	-0.14	0.17	-0.58	-0.59	0.13
Frost days	-0.15	0.05	0.96	0.22	-0.08	0.00
Downy mildew	-0.44	0.32	0.11	-0.75	0.28	-0.23
Powdery mildew	-0.10	0.83	-0.15	0.19	-0.50	0.03
Weight	0.53	0.22	0.16	0.07	0.01	0.00

Bioclimatic indices without temperature correction						
Huglin index	0.55	0.18	0.08	0.07	-0.20	-0.79
Flavescence dorée	0.50	0.35	0.17	-0.08	-0.53	0.56
Extreme heat days	0.50	-0.18	0.08	-0.59	0.59	0.11
Frost days	-0.10	-0.18	0.96	0.15	0.05	-0.02
Downy mildew	-0.43	0.32	0.14	-0.75	-0.27	-0.21
Powdery mildew	-0.07	0.83	0.08	0.21	0.51	0.03
Weight	0.52	0.23	0.16	0.07	0.01	0.00

Physical parameters					
Daily mean temperature	0.51	0.27	0.04	0.01	-0.81
Daily minimum temperature	0.48	0.43	-0.04	0.62	0.45
Daily maximum temperature	0.52	0.14	0.10	-0.75	0.37
Precipitation	-0.35	0.54	0.76	-0.04	-0.00
Relative humidity	-0.34	0.66	-0.64	-0.21	-0.02
Weight	0.71	0.17	0.11	0.01	0.00

Tab. S3.1 Principal Components (PC) and explained variance for three variable sets: bioclimatic indices with and without temperature corrections respectively, and raw physical parameters with temperature corrections

The first principal component (PC1), accounting for 53% of the total variance, is primarily driven by temperature-related indices such as the Huglin index, the flavescence dorée index, and the number of extreme heat days, while it is negatively correlated with the downy mildew index. The second component (PC2), capturing 22% of the variance, is

predominantly influenced by the powdery mildew index. The third component (PC3) has a weight of 0.16, and mainly reflects the number of frost days, negatively correlated with the powdery mildew index. It makes sense, as powdery mildew thrives in warmer temperatures, whereas frost is associated with colder conditions that would inhibit the development of the pathogen. PC3 appears to be stringy, because it primarily represents the number of frost days, a count-based variable with small values, with most regions showing a value of zero. The fourth, fifth, and sixth components each have minimal contribution, with weights below 0.07. Thus, PCA reduces the number of effective degrees of freedom from six to three while preserving the most relevant information.

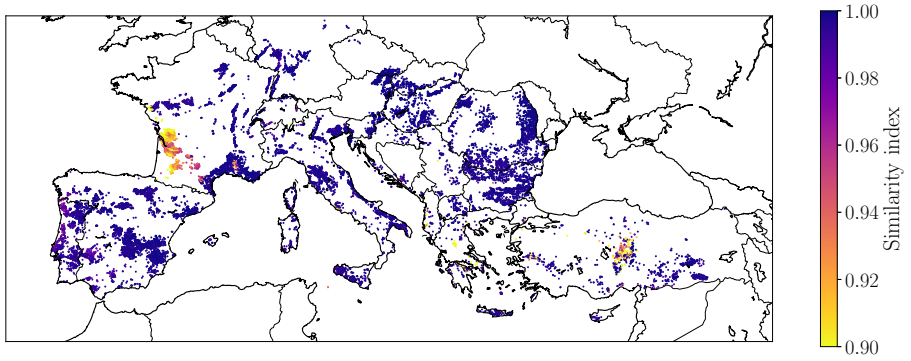

Fig. S3.1 Map of the similarity index of the best analogue of each European vineyards

Fig. S3.1 presents the similarity index of the best analogue of all European vineyards. Most vineyards show very high analogue similarity (92% of cases with $SI \geq 0.9$), though a few outliers have values as low as 0.2. The lower similarities mainly occur in Bordeaux, southwestern France, and northern Anatolia—regions expected to face more spring frost events due to earlier bud break. Because the frost index distribution is highly skewed toward zero, rare high values can disproportionately affect analogue selection. In contrast, all other regions successfully identify close climatic analogues for future conditions.

S4 Alternative methods of indices aggregation

S4.1 Mahalanobis distance

As explained in Section 2.3, we use SED on principal components to aggregate indices while compensating for correlations between them, that would otherwise yield to overweight some data as compared to others. Here, we discuss an alternative technique to aggregate indices used in climate analogues computations, namely the Mahalanobis distance (MD). This distance is computed using the covariance matrix of the dataset, making it sensitive to the shape and spread of the data distribution, and to correlations between indices (Bulut et al., 2025). It is given by:

$$MD_{ij}^2 = \sum_{k=1}^{N} \left(\frac{p_{ik} - f_{jk}}{s_j} \right)^T R_j^{-1} \left(\frac{p_{ik} - f_{jk}}{s_j} \right) \tag{S4.1}$$

with p_{ik} is the value of index k at the grid point i in the current climate, f_{jk} is the value of index k at the vineyard location in the future climate, s_j is the spatial standard deviation of the index among the vineyards and R_j the $N \times N$ correlation matrix of the indices in the future dataset. Spatial normalisation is also considered here.

However, this method is not suitable for the problem at hand. While MD is effective for computing the distance between a point and a dataset, it has limitations in our context, where we calculate distances between pairs of individual points. By taking into consideration the inverse correlation matrix, MD gives more weight to components with smaller variability. This approach makes sense when the variables with the greatest variability are considered to be noisy and therefore less meaningful. However, in the case under consideration, the variables with the greatest spatial variability are the key factors that distinguish the climates of different regions and, therefore, should be weighted more heavily. In fact, MD is equivalent to the Euclidean distance applied to the principal components, but with weights inversely proportional to their explained variance. This results in components with the least explanatory power (i.e., the least physical meaning and largest noise in the relevant use cases of MD) having the greatest influence on the distance calculation—an approach that contradicts the desired behaviour

In contrary, the Mahalanobis distance would be relevant if year-to-year temporal distributions were considered for each vineyard rather than only means of each index over the considered period. For each vineyard, one could compute the distance between a present-day point and the temporal distribution of the thirty future points corresponding to the vineyard's future thirty-year period. However, this method would require working with yearly data rather than averages over thirty-year periods, making the computations and storage requirement much more demanding. Therefore, this approach is not utilized in the current study.

S4.2 Wasserstein distance

When tackling the problem of regions matching, in Section 2.4, we assessed the relevance of the Wasserstein distance (WD), a distance function defined between probability distributions (Bulut et al., 2025):

$$WD^2_{(\mu,\nu),k} = \inf_{\gamma_{i,j}} \sum_{j\in A,\ i\in B} \gamma_{i,j} \left[d(p_{ik}, f_{jk}) \right], \tag{S4.2}$$

where μ and ν are two discrete distributions to be compared (in our case, the present climate indices in region A in the future and in region B in the present), p_{ik} is the value of index k for the grid point i in the present climate, f_{jk} is the value of index k for the vineyard j in the future climate, and $\gamma_{i,j}$ are the transport plan coefficients describing how the mass transports from p_{ik} to f_{jk}. The notation $\inf_{\gamma_{i,j}}$ represents the infimum over the set of possible values for $\gamma_{i,j}$. Finally $d(p_{ik}, f_{jk})$ is a distance between the two values for the considered parameter. In our case, d is the PCA-weighted SED described in Section 2.3. The total distance between two regions is computed by summing the Wasserstein distance between the two distributions of each index.

However, this method tends to match regions not only based on their average climate indices, but also on the similarity of their entire distributions. The latter conditions induces strong biases in our sample. Indeed mountainous regions intrinsically have larger dispersion than those with flatter topography, especially when sub-grid temperature correction is considered. Furthermore, our approach for defining prospective vine-growing regions tends to overestimate climate variability, as these areas are not restricted to the climatically favourable locations that characterize existing vineyards.

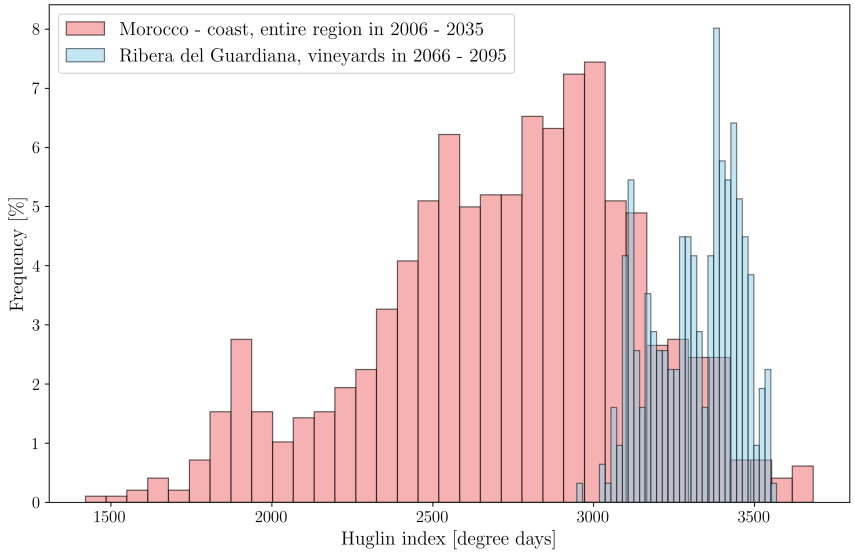

Fig. S4.1 Distributions of the Huglin index for the Morocco - Coast region in 2020, and of vineyards located in the Ribera del Guardiana region in 2080

For example, the Ribera del Guadiana region in Spain finds most of its analogues in the Morocco - Coast region. However, a comparison of their index distributions reveals a significant mismatch between the distributions. Fig. S4.1 shows the distribution of the Huglin index for vineyard locations in Ribera del Guadiana during 2080, alongside the distribution of the Huglin index for the entire Morocco - Coast region in 2020. The figure highlights that only a small subset of the Morocco - Coast region aligns with the vineyard distribution. This discrepancy arises because the Morocco - Coast region is highly heterogeneous in terms of climate, encompassing desert areas, coastal zones, and mountainous regions. This results in a broad spread of the Huglin index, a characteristic not observed in the more homogeneous distribution of vineyards.

One way to partially address this issue is by restricting each region to a subset of potential vineyards, i.e. to points that are at least once identified as a analogue of any European vineyard (points in Fig. 5). This approach ensures that areas such as mountains, lakes, or deserts are excluded from the distribution. However, it does not fully resolve the issue of regional homogeneity. Even when focusing solely on potential vineyards, a region may still encompass diverse climates, corresponding to analogues from multiple distinct regions, leading to distributions that remain significantly broader than those of the future

vineyards. Consequently, the Wasserstein distance method sometimes pairs regions in a way that does not meet our requirement that a region B hosting most of the analogues of region A should be identified as its analogue region. In some cases, it even assigns analogue regions that contain no vineyard analogues at all while overlooking regions that contain the majority of them. For example, while over 99% of the vineyard analogues for the Champagne region are located in Bordeaux and the South-West of France, the Wasserstein approach identifies the Upper Danube Valley and the Podravska regions as the analogue regions for Champagne. This highlights a fundamental limitation of the Wasserstein distance approach in effectively matching wine regions due to its sensitivity to distribution width.

S5 Effect of the number of retained analogues on the region analogues

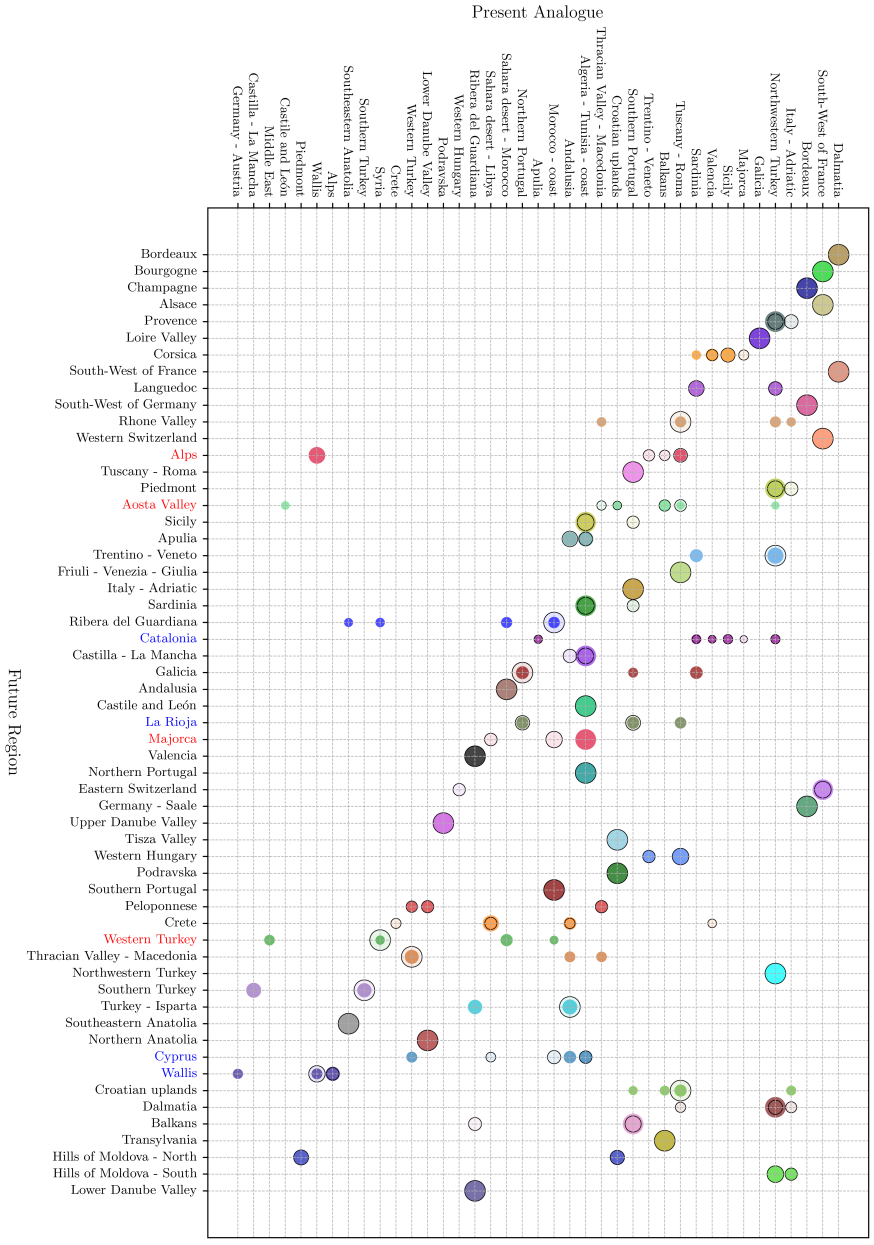

Fig. S5.1 Regions matches between the projected climate of vine-growing regions (left) and their analogue regions in the present (top). The area of the dot is proportional to the score of the analogue region. Dark circles: using 20 analogues per vineyard; light circles: using 5 analogues per vineyard. Black future regions: same analogue region; Blue future regions: different top analogue $\leq$ 500 km apart; red future regions: different top analogue $>$ 500 km apart

S6 Impact of temperature corrections on the bioclimatic indices

Fig. S6.1 shows the correction to the mean daily temperature on May 15, 2006 at each vine location. While the slope-related correction (Eq. 2.2) varies throughout the year, the elevation correction (Eq. 2.1) remains constant. Although the figure displays corrections caped to $[-2°C, 2°C]$, some vineyards in Alpine regions can experience adjustments exceeding $+10°C$, primarily due to elevation-related corrections in deep valleys. Furthermore, corrections of around $\pm 1°C$ or more are common across the domain, highlighting the necessity of these adjustments to accurately represent microclimatic variations at vineyard sites.

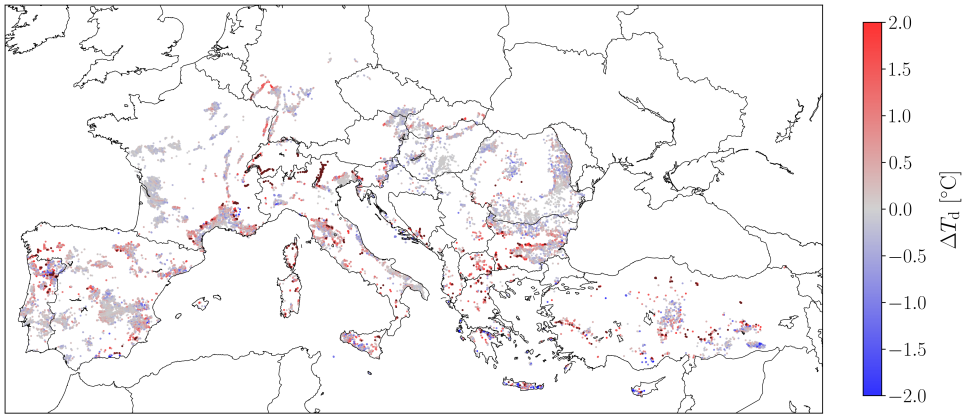

Fig. S6.1 Correction to the daily average temperature of European vineyards due to topography (elevation and slope) on May 15, 2006. Dark red dots indicate locations where the correction exceeds $+2°C$

The temperature correction for topography directly impacts all bioclimatic indices, whether related to the vine development or to pathogens. We investigate the variation of each index when the corrections are taken into account.

Fig. S6.2a illustrates the effect of temperature corrections on the Huglin index for 2020, with values ranging from -1000 to $+1500$ degree-days, and 90% within ± 200 degree-days. The most affected areas are the Alps and the Wallis region, spanning Switzerland and northern Italy, all with a positive correction. Thus, without accounting for temperature adjustments, certain areas would not meet the necessary conditions for successful viticulture, because there would be either too cold or too hot. Results are similar for 2080. The corrections to the flavescence dorée index, displayed in Fig. S6.2b, are similar to those of the Huglin index, since both indices are computed using a degree-day method. However, the scale of the correction differs between the two indices due to variations in the base temperature and the time period considered. Corrections range from -2000 to $+2000$ degree-days, with 95% of values falling within ± 400 degree-days. This corresponds to nearly half a generation (with one generation requiring 1035 degree-days (I.E. et al., 2011)). Consequently, these corrections significantly impact the risk of infection, which increases exponentially with the number of generations. For both indices, the corrections are consistent with the temperature corrections shown in Fig. S6.1.

Since the frost index only depends on the daily minimum temperature (Eq. S2.3), it is only impacted by temperature corrections due to elevation. For most vineyards, the number of frost days during the growing season is minimally affected by temperature adjustments as seen in Fig. S6.2c. The plot has been caped to ±0.1 days per year, which contains 99% of vineyards, although values ranges from −55 to +0.16 days per year. Indeed, in the Alps and the Wallis regions, the number of frost days decreases by up to 55 days per year in 2020, reflecting only negative corrections (i.e., fewer frost days after temperature adjustments) due to higher temperatures during the growing season. A smaller difference in the number of frost days, both positive and negative, is observed in Northern Bulgaria and central Italy, with corrections of the order of one event every second years. In 2080, the differences persist in the Alpine regions but are significantly smaller. The number of frost days in the Alps during this period reaches a maximum of 3.5 days without temperature correction and drops to zero across the entire region when corrections are applied.

The impact of temperature correction on the number of extreme heat days for 2020 is shown in Fig. S6.2d. 96% of values are within ±2 days per year, so that the plot is capped to this range. The Iberian Peninsula, Sicily, and Turkey are the most affected areas, with differences up to −20 days per year in southeastern Turkey. This region is characterised by a complex terrain, where elevation differences between two points in the same grid cell can be significant. In such regions, temperature correction is essential for accurately modelling

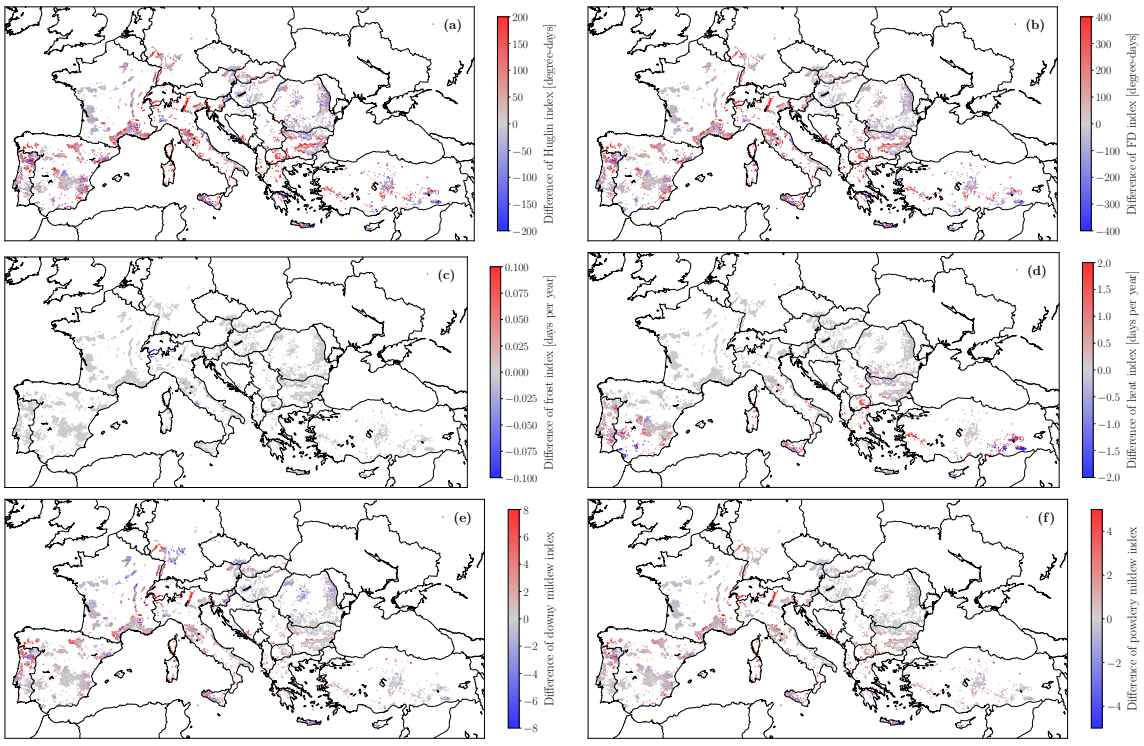

Fig. S6.2 Difference of indices values with and without temperature correction of European vineyards in 2020. **(a)** Huglin index; **(b)** Flavescence dorée index; **(c)** Frost days index; **(d)** Extreme heat index; **(e)** Downy mildew index; **(f)** Powdery mildew index

vine growth. Notably, in some areas, such as Greece and southwestern Turkey, temperature correction increase the number of extreme heat days. In 2080, these differences become more pronounced, generally ranging between −10 and 10 days and up to −30 to +40 days per year.

The number of risk days for downy mildew infection is displayed in Fig. S6.2e. For 97% of vineyards, the correction remains within ±8 days at risk per year, with all corrections falling within ±20 days. The risk of infection increases by approximately 5 days in regions such as northern Portugal, Sicily, and Alsace when temperature corrections are applied. In the Alps and Wallis regions, this correction can reach up to 25 days as compared to a base value of about 30 days without temperature correction. This increase is due to the crossing of the threshold $T_d \geq 12°C$ (Eq. S2.8). Once again, the results align with the temperature corrections shown in Fig. S6.1. Conversely, the risk of infection decreases by about 5 days in southeastern Germany, Champagne and northern Romania, where temperature corrections are slightly negative. The powdery mildew index shows minimal sensitivity to temperature corrections (Fig. S6.2f), with values within ±18 risk days per year, and 99% within ±5 days per year. A notable exception is found in the Alps, Wallis and northern Italy, where the number of risk days increases by about 10 days due to higher temperatures.

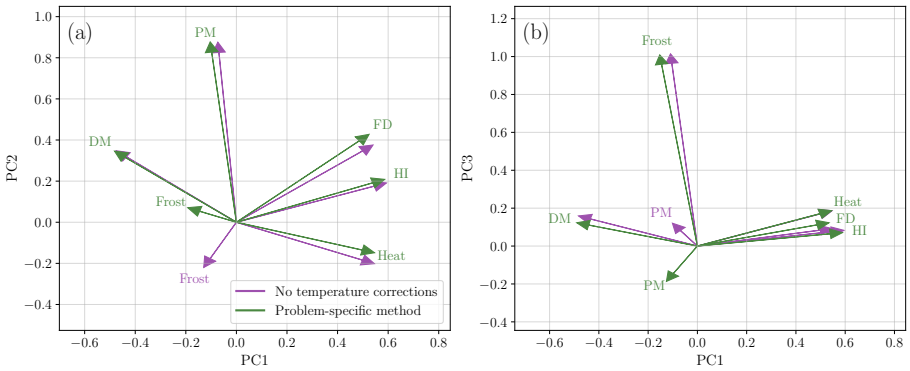

Fig. S6.3 Contribution of each index to the first three principal components computed from the six bioclimatic indices with and without topographic temperature corrections. (a) PC1 vs PC2 and (b) PC1 vs PC3. HI: Huglin index, FD: flavescence dorée index, Frost: frost days index, Heat: heat days index, DM: downy mildew index, PM: powdery mildew index

Fig. S6.3 shows the contribution of each index to the first three principal components, calculated with and without temperature corrections. Overall, the corrected and uncorrected versions of each index contribute similarly to the PC. This outcome is expected because corrected and uncorrected indices are strongly correlated. Two exceptions stand out: the frost index contributes more to PC2 without temperature corrections, and the powdery mildew index contributes more to PC3 when corrections are applied. However, both remain relatively minor contributors in absolute terms. The PC obtained from the bioclimatic indices without temperature corrections are found in in Tab. S3.1.

S7 Effect of each methodological improvement on the analogue selection

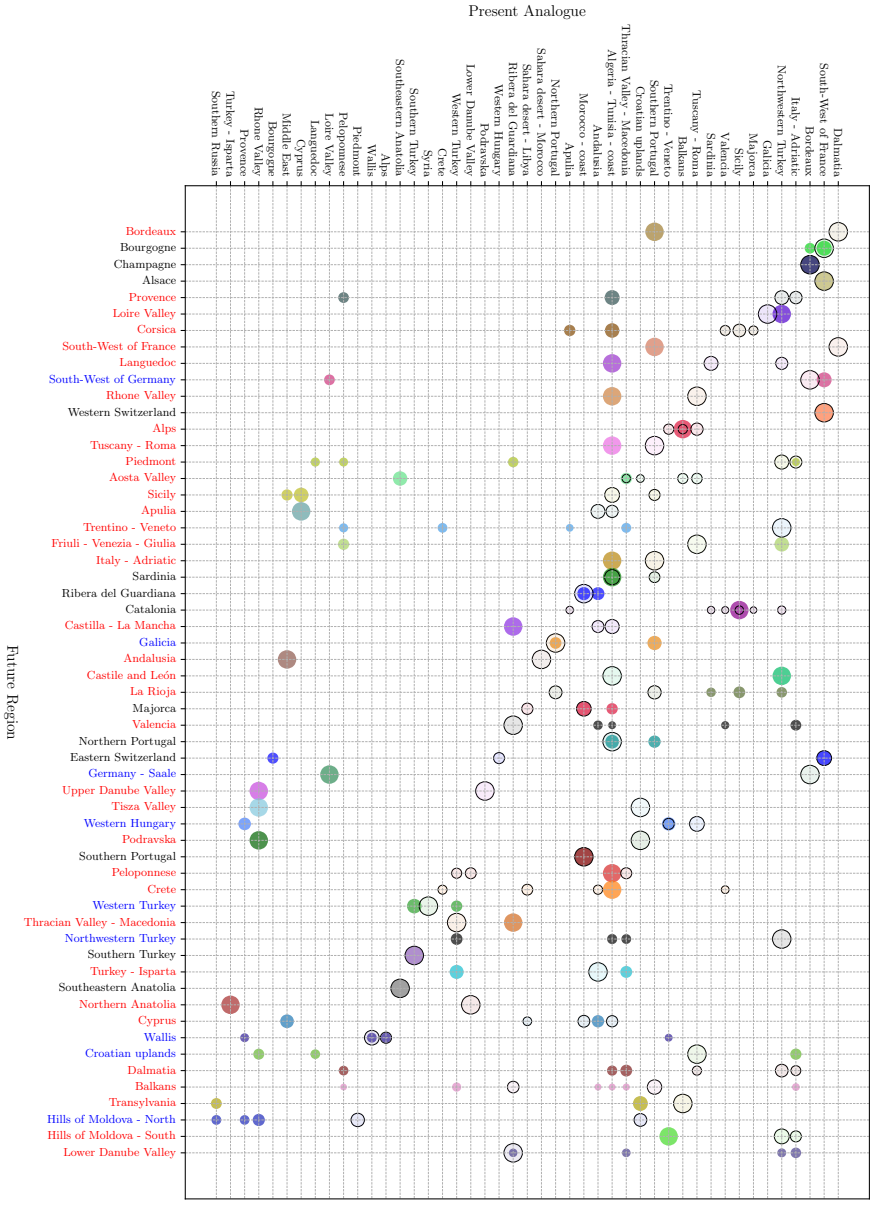

Fig. S7.1 Regions matches between the projected climate of vine-growing regions (left) and their analogue regions in the present (top). The area of the dot is proportional to the score of the analogue region. Dark circles: generic method; light circles: problem-specific. Black future regions: same analogue region; Blue future regions: different top analogue $\leq$ 500 km apart; red future regions: different top analogue $>$ 500 km apart.

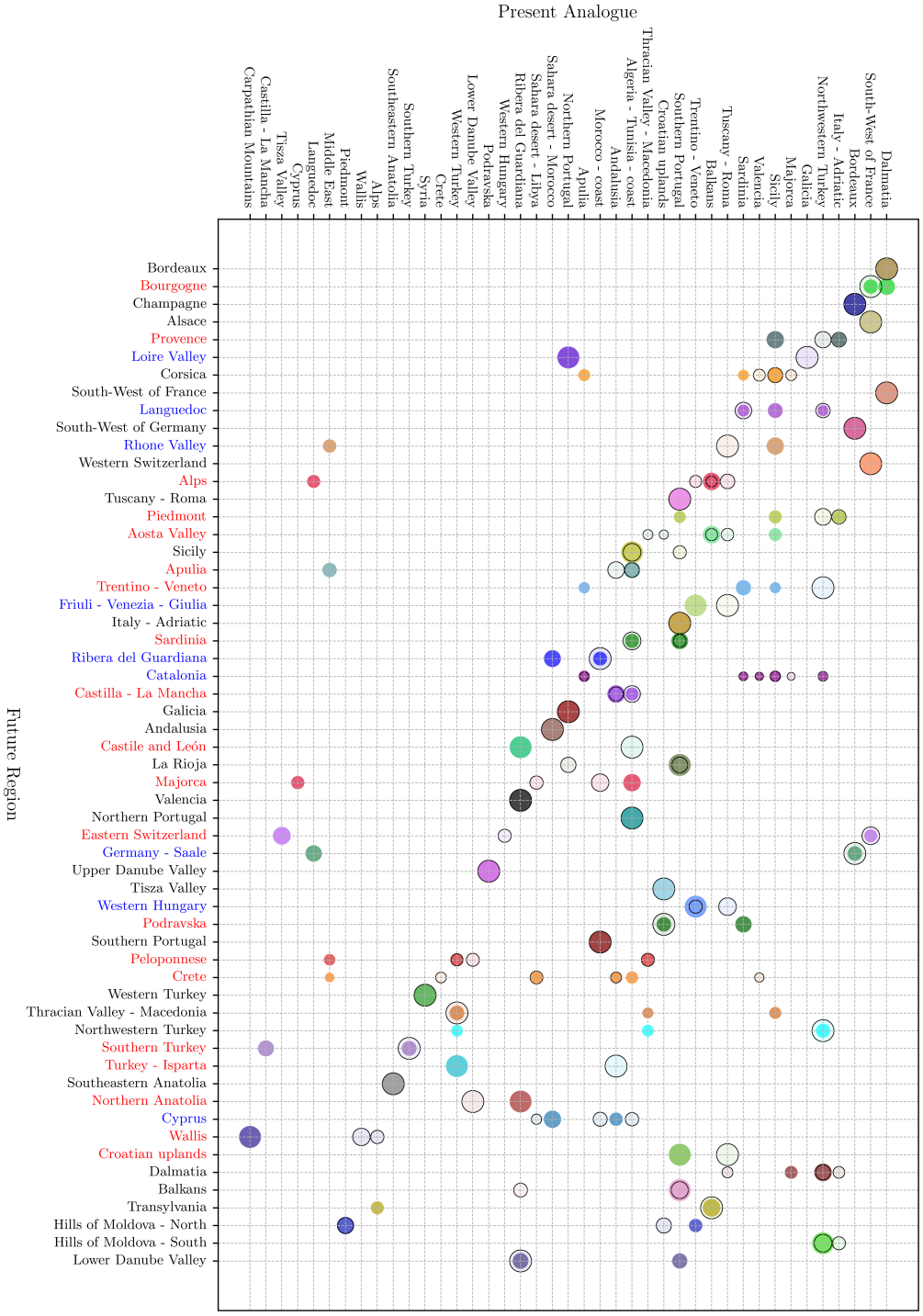

Fig. S7.2 Regions matches between the projected climate of vine-growing regions (left) and their analogue regions in the present (top). The area of the dot is proportional to the score of the analogue region. Dark circles: without temperature corrections; light circles: with temperature corrections. Black future regions: same analogue region; Blue future regions: different top analogue $\leq$ 500 km apart; red future regions: different top analogue $>$ 500 km apart

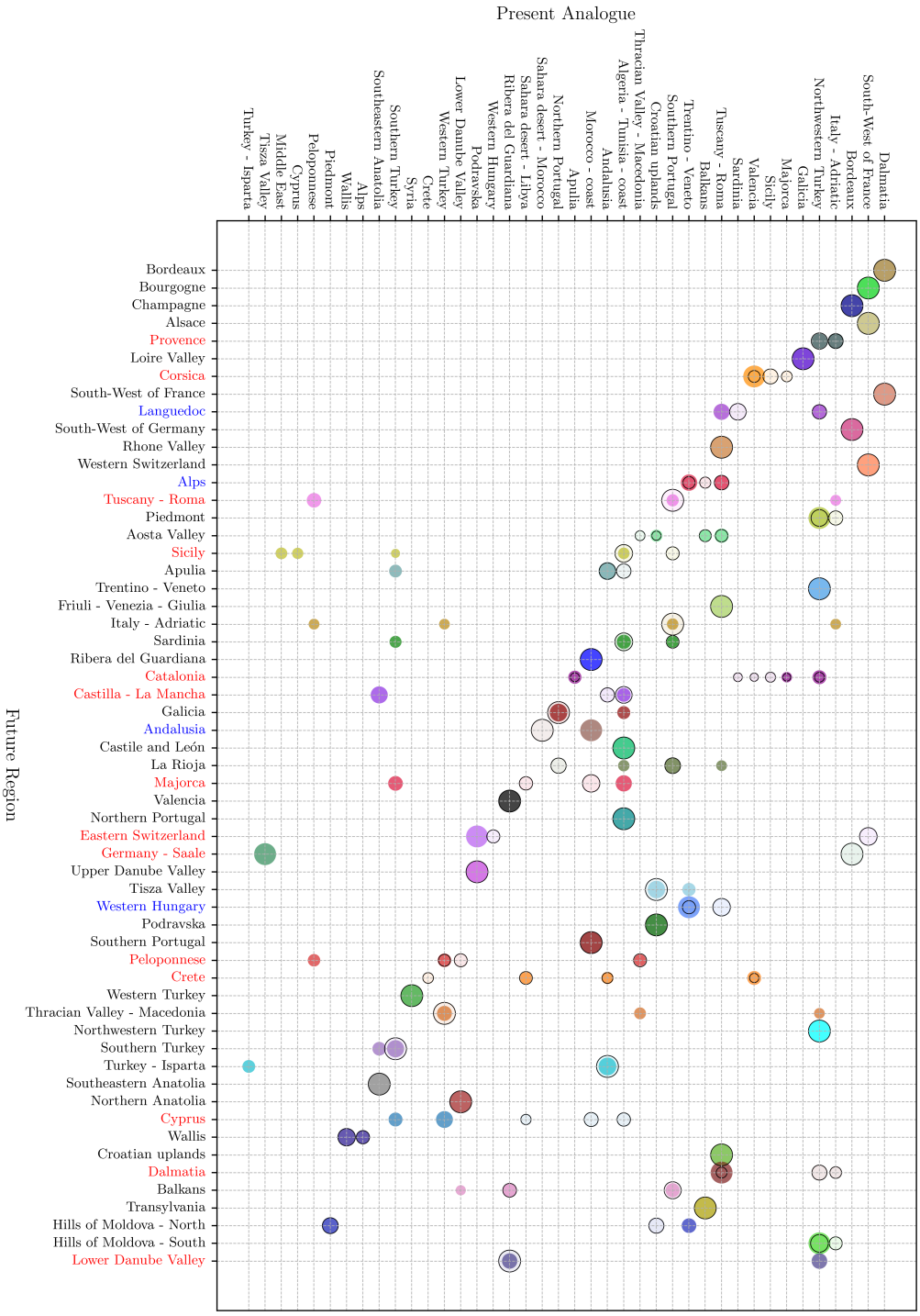

Fig. S7.3 Regions matches between the projected climate of vine-growing regions (left) and their analogue regions in the present (top). The area of the dot is proportional to the score of the analogue region. Dark circles: without PCA; light circles: with PCA. Black future regions: same analogue region; Blue future regions: different top analogue $\leq$ 500 km apart; red future regions: different top analogue $>$ 500 km apart

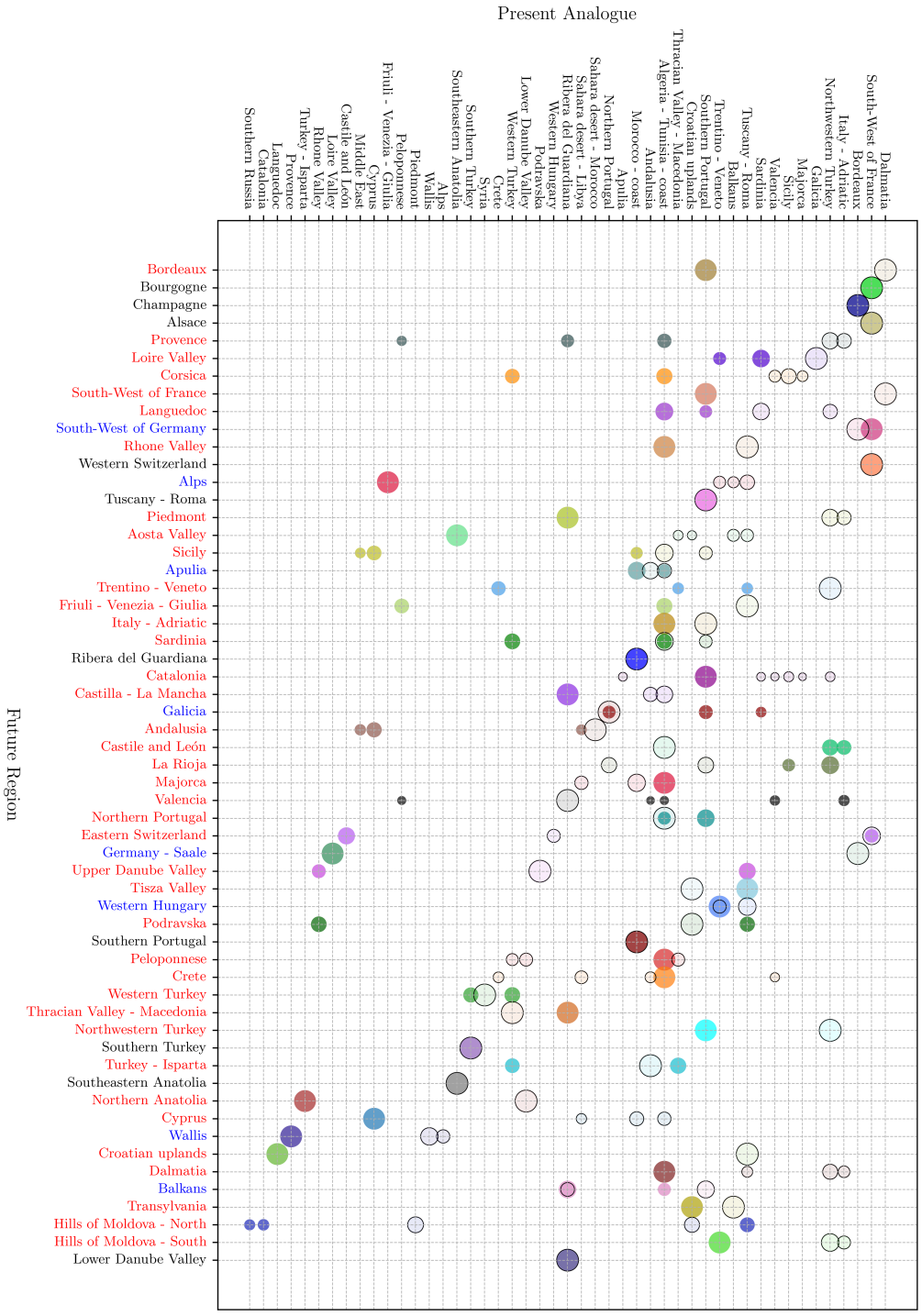

Fig. S7.4 Regions matches between the projected climate of vine-growing regions (left) and their analogue regions in the present (top). The area of the dot is proportional to the score of the analogue region. Dark circles: using physical parameters; light circles: using bioclimatic indices. Black future regions: same analogue region; Blue future regions: different top analogue $\leq$ 500 km apart; red future regions: different top analogue $>$ 500 km apart

References

J. Bennie, B. Huntley, A. Wiltshire, M. O. Hill, and R. Baxter. Slope, aspect and climate: Spatially explicit and implicit models of topographic microclimate in chalk grassland. *Ecological Modelling*, 216(1):47–59, 2008. ISSN 0304-3800. doi:https://doi.org/10.1016/j.ecolmodel.2008.04.010.

B. Bulut, M. Vrac, and N. de Noblet-Ducoudré. What Will the European Climate Look Like in the Future? A Climate Analog Analysis Accounting for Dependencies Between Variables. *Earth's Future*, 13, 2025. doi:https://doi.org/10.1029/2024EF004972.

J. Carroll and W. Wilcox. Effects of Humidity on the Development of Grapevine Powdery Mildew. *Phytopathology*, 93:1137–44, 2003. doi:https://doi.org/10.1094/PHYTO.2003.93.9.1137.

J. Duffie and W. Beckman. *Solar Engineering of Thermal Processes*. John Wiley & Sons, Ltd, 2013. doi:https://doi.org/10.1002/9781118671603.fmatter.

I. Garcia de Cortazar-Atauri, N. Brisson, and J. Gaudillere. Performance of several models for predicting budburst date of grapevine (Vitis vinifera L.). *International Journal of Biometeorology*, 53:317–26, 2009. doi:https://doi.org/10.1007/s00484-009-0217-4.

A. Hall and G. Jones. Spatial analysis of climate in winegrape-growing regions in Australia. *Australian Journal of Grape and Wine Research*, 16(3):389–404, 2010. ISSN 1322-7130. doi:https://doi.org/10.1111/j.1755-0238.2010.00100.x.

T. Holmes, W. Crow, and C. Hain. Spatial patterns in timing of the diurnal temperature cycle. *Hydrology and Earth System Sciences*, 17(10), 2013. doi:https://doi.org/10.5194/hess-17-3695-2013.

P. Huglin. *Biologie et écologie de la vigne*. Paris : Lavoisier - Tec & doc, 2003. ISBN 978-2-7430-0260-2.

R. I.E., M. Jermini, D. Fuog, and J. Baumgärtner. Towards an improved understanding of the dynamics of vineyard-infesting Scaphoideus titanus leafhopper populations for better timing of management activities. *Pest management science*, 67:1222–9, 2011. doi:https://doi.org/10.1002/ps.2171.

H. Kambezidis. An in-depth analysis of two common methodologies used to derive hourly solar radiation values from daily ones: pros and cons. *Frontiers in Environmental Science*, 13, 2025. doi:https://doi.org/10.3389/fenvs.2025.1528355.

T. Oke. *Boundary Layer Climates*. Routledge, 1987. ISBN 9780415043199. URL https://books.google.ch/books?id=K_2dW7crfVIC.

J. P. Peixoto and A. H. Oort. 7. Observed Mean State of the Atmosphere. In *Physics of Climate*, pages StartPage–EndPage. American Institute of Physics, New York, NY, USA, 1992. URL https://www.osti.gov/biblio/7287064.

P. Pieri and J. P. Gaudillère. Sensitivity to training system parameters and soil surface albedo of solar radiation intercepted by vine rows. *VITIS - Journal of Grapevine Research*, 42(2):77, 2015. doi:https://doi.org/10.5073/vitis.2003.42.77-82.

B. Sneiders, D. Fleury, and S. Goyette. Influence du réchauffement climatique sur la dynamique des populations de Scaphoideus titanus en Romandie. *Revue suisse Viticulture, Arboriculture, Horticulture*, 2019.

K. B. Walter Kast. The expert system OiDiag-2.2. - a useful tool for the precise scheduling of sprays against powdery mildew of vine (Erysiphe necator Schwein.). *State Institute for Viticulture, Oenology and Fruit Technology*, 2009.

M. Wann, D. Yen, and H. J. Gold. Evaluation and calibration of three models for daily cycle of air temperature. *Agricultural and Forest Meteorology*, 34(2):121–128, 1985. ISSN 0168-1923. doi:https://doi.org/10.1016/0168-1923(85)90013-9.

S. Zito, T. Castel, Y. Richard, M. Rega, and B. Bois. Optimization of a leaf wetness duration model. *Agricultural and Forest Meteorology*, 291:108087, 2020. ISSN 0168-1923. doi:https://doi.org/10.1016/j.agrformet.2020.108087.